Petroleum Science 23 (2026) 2188–2204

Contents lists available at ScienceDirect

Petroleum Science

journal homepage: www.keaipublishing.com/en/journals/petroleum-science

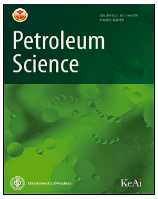

Original Paper

Effects of swelling clay layers on fluid production from hydrate-bearing sediments induced by depressurization

Junjie Ren [a,b], Hongfeng Lu [a], Chenlu Xu [a], Junjie Zheng [c], Yue Zhang [c], Yunting Liu [b], Praveen Linga [c], Zhenyuan Yin [a,b,*]

[a] *National Engineering Research Center of Gas Hydrate Exploration and Development, Guangzhou Marine Geological Survey, China Geological Survey, Guangzhou, 511458, Guangdong, China*
[b] *Institute for Ocean Engineering, Tsinghua Shenzhen International Graduate School, Tsinghua University, Shenzhen, 518055, Guangdong, China*
[c] *Department of Chemical and Biomolecular Engineering, National University of Singapore, 117585, Singapore*

A R T I C L E I N F O

Article history:
Received 4 May 2025
Received in revised form
5 November 2025
Accepted 12 March 2026
Available online 17 March 2026

Edited by Min Li

Keywords:
CH_4 hydrate
Natural gas hydrate
Gas hydrate
Montmorillonite
Fluid production
CH_4 recovery

A B S T R A C T

Clay-rich sediments are common in natural gas hydrate reservoirs and pose significant technical challenges in past field production tests. Among these, Na-montmorillonite significantly affects methane hydrate (MH) formation and dissociation due to its swelling and water absorption properties. However, the role of swelling clay layers on fluid production by depressurization remains unclear, thus limiting CH_4 recovery efficiency. This study aims to elucidate the role of swelling clay on fluid production from natural gas hydrate deposits under depressurization. We synthesized MH-bearing sediments in the presence of sand, clay, and clay-sand alternating layers to examine fluid production and water-gas ratios under different bottom-hole pressures of 6.0 and 10.0 MPa. Results suggest that MH formation rates and final saturation are significantly lower in clay layers (14%) compared to sand layers (29%). During depressurization, MH in clay layers decomposed earlier due to the thermodynamic inhibitory effects of Na-montmorillonite. Swelling clay reduced water recovery (4.3%) and increased gas recovery (88.4%) in clay-sand layers at 6.0 MPa. Lowering pressure enhanced CH_4 recovery to 88.4% in clay, 71.8% in clay-sand, and 68.3% in sand layers. Depressurization created persistent low-temperature region in clay layers ($\Delta T = 2.0\ ^{\circ}C$), potentially promoting MH reformation. Heat conduction was more dominant in sand layers than clay layers, indicating imbalance interlayer heat transfer characteristics. These findings offer critical insights for optimizing depressurization strategies in clay-rich hydrate reservoirs, enabling secure and efficient energy recovery from clay-rich NGH deposits.

1. Introduction

The global transition towards natural gas as a cleaner energy source is primarily driven by its relatively lower CO_2 emissions, which are approximately half those of other fossil fuels (Gürsan and de Gooyert, 2021; Kotchen and Mansur, 2016; Li et al., 2025). According to the World Energy Outlook 2023, global natural gas demand is projected to exceed 4200 billion cubic meters by 2030, posing significant supply challenges, particularly for rapidly developing nations like China. To meet this rising demand, alternative gas resources such as natural gas hydrates (NGH) have gained ever-increasing attention.

NGH deposits contain nearly twice the amount of organic carbon found in all conventional fossil fuels combined (Cheng et al., 2026), making them a promising energy source. Successful production tests in the Nankai Trough (Japan) and the South China Sea (China) have demonstrated their technical feasibility (Li et al., 2018; Qin et al., 2020; Yamamoto et al., 2019). However, over 90% of NGH reserves are located in deep-sea clay-rich sediments (water depths >1000 m), where commercial production faces major technical and economic challenges. Offshore NGH production tests in both the Nankai Trough and the Shenhua area encounter similar difficulties (see Fig. 1). These field tests

---

* Corresponding author.
E-mail address: zyyin@sz.tsinghua.edu.cn (Z. Yin).
Peer review under the responsibility of China University of Petroleum (Beijing).

https://doi.org/10.1016/j.petsci.2026.03.029
1995-8226/

Nomenclature

n_{G}	Number of moles of gas phase, mol
n_{H}	Number of moles of CH_4 hydrate phase, mol
n_{W}	Number of moles of water, mol
P_{eq}	Phase equilibrium pressure of CH_4 hydrate, MPa
P_{GR}	Pressure of gas reservoir, MPa
P_{top}	Pressure of reactor, MPa
P_{well}	Pressure of well, MPa
R_{G}	Recovery ratio of CH_4 gas, %
R_{W}	Recovery ratio of water, %
S_{G}	Gas saturation, %
S_{H}	CH_4 hydrate saturation, %
S_{W}	Water saturation, %
t_{90}	Time required for 90% CH_4 conversion during MH formation, h
T_{avg}	Average temperature of the reactor, K
T_{bath}	Temperature of water in the circulating chiller, K
t_{D90}	Time required for 90% CH_4 gas recovery, h
V_{G}	Volume of gas phase, mL
V_{GLS}	Volume of gas-liquid separator, mL
V_{GR}	Volume of gas reservoir, mL
V_{MH}	Volume of CH_4 hydrate phase, mL
V_{R}	Volume of reactor, mL
V_{W}	Volume of water, mL
X_{CH_4}	Conversion of CH_4 to CH_4 hydrate, %
Z	Compressibility factor
ρ_{G}	Molar volume of gas phase, cm^3/mol
ρ_{MH}	Molar volume of CH_4 hydrate phase, cm^3/mol
ρ_{W}	Molar volume of water, cm^3/mol
Φ	Porosity of sediments, %
CBW	Clay-bound water
Na-MMT	Sodium montmorillonite
WGR	Water-to-gas ratio, mol/mol

underscore the complex role of clay in gas recovery from clay-rich methane hydrate-bearing sediments (MHBS). In the Nankai Trough, MHBS is characterized by alternating clay and sand layers, with sheet-like sequences containing more than 20 layers ranging from 30 to 70 cm in thickness (see Fig. 1(c)). Logging data indicate that MH saturation (S_{H}) in clay layers ($S_{\mathrm{H}} = 0\%$–10%) is significantly lower than that in adjacent sand layers ($S_{\mathrm{H}} = 50\%$–80%) (Fujii et al., 2015), suggesting that clay exerts a substantial influence on water and gas accumulation as well as recovery pathways in NGH reservoirs.

A key challenge lies in understanding the fluid production behavior of clay-rich NGH reservoirs. Sediments in major hydrate-bearing regions—including the Nankai Trough (Japan), Krishna-Godavari Basin (India), and Shenhu area (South China Sea)—are dominated by montmorillonite, illite, kaolinite, and chlorite (Fujii et al., 2015; Yadav et al., 2019; Yoneda et al., 2015; Yu et al., 2019). These clay minerals possess fine particle sizes (<4 μm), high specific surface areas (up to 800 m^2/g), pronounced swelling behavior, and inherently low permeability, all of which contribute to complex multiphase flow during production (Liu et al., 2023a; Yamamoto et al., 2019). Critically, clay minerals also thermodynamically inhibit MH formation. For example, Sodium montmorillonite (Na-MMT) reduces the phase equilibrium temperature (T_{eq}) by ~4 K (Ren et al., 2024). Moreover, during MH dissociation, the absorbed water causes Na-MMT to swell, forming a low-permeability layer that effectively traps the dissociated water (Ren et al., 2022b). Despite these clear implications, the influence of clay presence on gas recovery from clay-rich MHBS remains insufficiently understood. Most existing studies have primarily focused on sandy hydrate-bearing sediments, leaving the role of clay in governing production behavior largely unexplored and often speculative.

Depressurization remains the most viable method for NGH production, as demonstrated in multiple offshore production tests (Yamamoto et al., 2019; Ye et al., 2020). However, clay-rich sediments introduce several unique complications that hinder fluid

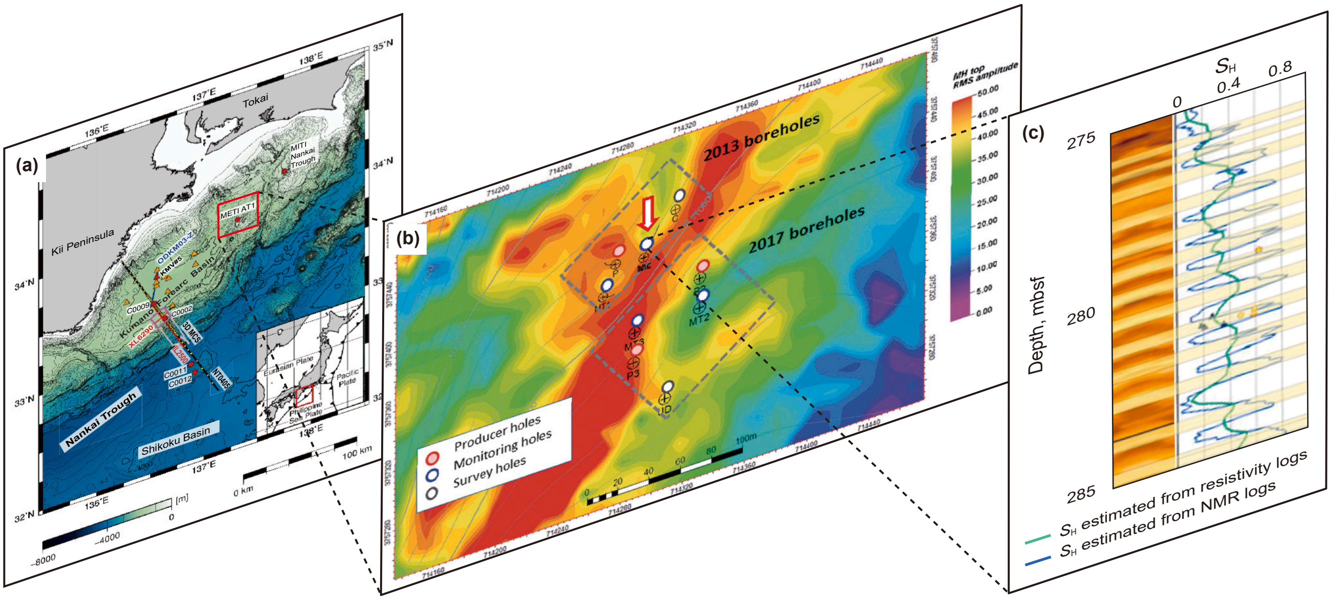

Fig. 1. **(a)** Map of survey locations in the eastern Nankai Trough, Japan (reproduced with permission from Shiraishi et al. (2019)); **(b)** location of the 2013 and 2017 offshore production test sites, including the production and monitoring wells (reproduced from Yamamoto et al. (2019)); **(c)** logging data from the AT1-MC well compared with core analyses from the AT1-C well (reproduced with permission from Fujii et al. (2015)).

production efficiency. Field observations from the 2013 Nankai Trough production test revealed unstable pressure control, during which the bottom-hole pressure (BHP) dropped abruptly to 5.0 MPa and remained stalled for 98 h (Konno et al., 2017). In addition, the inherently low permeability of clay-rich layers severely restricts fluid flow, resulting in limited water production and reduced well productivity (Yamamoto et al., 2019). These operational challenges are further compounded by technical limitations in reservoir characterization. Conventional imaging and diagnostic techniques, such as X-ray CT and NMR cannot adequately resolve clay micropores or detect signals from clay-bound water (Sun et al., 2021; Yang et al., 2017).

Despite these significant challenges, current research lacks systematic comparisons of fluid production behavior between clay-rich and sandy hydrate-bearing sediments. This study addresses this critical knowledge gap through three main objectives: (1) to analyze MH formation and dissociation behavior in alternating clay-sand layered systems; (2) to compare fluid production behavior and water-gas ratios under bottom-hole pressures (BHPs) of 6.0 and 10.0 MPa; and (3) to investigate the spatiotemporal evolution of temperature and pressure during MH dissociation. These experiments provide comprehensive insights into the influence of clay-rich sediments on depressurization-based gas recovery, offering practical guidance for optimizing production strategies in clay-rich NGH reservoirs.

2. Experimental section

2.1. Experimental materials

Sodium montmorillonite (Na-MMT, purity >85%) and quartz sand (analytical grade) were purchased from Shanlinshiyu Mineral Products Co., Ltd. and Shanghai Macklin Biochemical Co., Ltd., respectively. The median diameters (D_{50}) of the quartz sand and Na-MMT were approximately 113.8 and 2.4 μm, respectively (see Fig. S1 in the Supporting Information), with corresponding densities of 2.68 and 2.65 g/cm^3. Lithological analyses indicate that sand-clay alternating layers typically exhibit particle sizes ranging from 4.0 to 146.4 μm, with coarser fractions predominantly falling within the 70–130 μm range (Ito et al., 2015). Based on these characteristics, quartz sand with a D_{50} of 113.8 μm was selected for the experiments, as it closely reflects the particle size distribution of natural sand layers in the eastern Nankai Trough, Japan. The morphology of dry and pre-wetted Na-MMT, as well as its swelling behavior, is shown in Figs. S2 and S3 in the Supporting Information. Deionized water was prepared in the laboratory.

2.2. Experimental apparatus

The experimental setup consisted of a reactor with a capacity of approximately 3.3 L, designed to withstand a maximum pressure of up to 16.0 MPa (Fig. 2(a)). Temperature control was achieved using an external circulating chiller. Three multi-point thermocouples (T_a, T_b, T_c; precision ±0.1 K) were installed inside the reactor to monitor temperature evolution during MH formation and dissociation. Water was injected at 275.2 K using a high-pressure syringe pump equipped with an integrated cooling system. The reactor was connected to a vertical production well integrated with a pressure-regulation system, which included a proportional-integral-derivative (PID) controller to precisely regulate the depressurization process and maintain a constant BHP. A 2.2 L gas-liquid separator (GLS) and a 3.8 L gas reservoir (GR) were used to collect the produced CH_4 gas and water. Data acquisition was performed at 20-s intervals through a dedicated monitoring system.

Three sediment-packing configurations were adopted (Fig. 3), based on the sand-clay alternation characteristic of the Nankai Trough (Fig. 1(c)): (1) clay layers (Cases-C1 and C2), (2) sand-clay alternating layers (Cases-CS1 and CS2), and (3) sand layers (Cases-S1 and S2). Na-MMT was pre-moistened by adding 40 g of water per 100 g of dried clay, yielding a gravimetric water content (GWC) of 40%. This pre-treatment step was necessary because dry Na-MMT did not allow uniform distribution of injected water, as confirmed through preliminary tests. Pre-moistening ensured effective water absorption and conversion into clay-bound water (CBW), allowing for a comparative analysis of MH formation between CBW and sand pore water in moistened sand.

2.3. Experimental procedure

To prepare the clay samples, dry clay was first weighed and placed in a container. Deionized water was then gradually added using a spray bottle to achieve a gravimetric water content (GWC) of 40%, while the mixture was continuously homogenized with an electric mixer to ensure uniform wetting and prevent localized water accumulation (see Fig. S2 in the Supporting Information). The moistened clay was then sealed in airtight bags and stored for over 24 h to allow sufficient water redistribution before use.

MHBS with a target methane hydrate saturation (S_H) of ~30% was prepared, followed by depressurization at bottom-hole pressures (BHPs) of 6.0 and 10.0 MPa to induce MH dissociation. MHBS with sand-clay alternating layers was created, and depressurization at 3.0 MPa/h was performed according to the procedure summarized in Figs. 4 and S6:

a) The reactor was thoroughly cleaned and dried.
b) Dried quartz sand was packed into the lower half of the reactor and compacted to a porosity of approximately 43%.
c) The upper half of the reactor was filled with pre-moistened Na-MMT (GWC = 40%) and compacted to a porosity of approximately 70%. The production well was then inserted, and the reactor was sealed.
d) CH_4 flushing at 1.0 MPa was carried out three times to remove residual air.
e) CH_4 was injected up to 10.3 MPa, and the chiller was set to $T = 293.2$ K. After 4 h stabilization, the temperature was lowered to $T = 275.2$ K to initiate MH formation.
f) Once pressure and temperature stabilized ($\Delta P < 20$ kPa/h), indicating completion of premixed-water conversion, the moles of MH (n_H), hydrate saturation (S_H), and CH_4 uptake in the clay layer were calculated.
g) Multiple water injections were performed to further promote MH formation until the target S_H (~30%) was reached.
h) The reactor temperature was then raised to $T = 285.2$ K to simulate natural reservoir conditions.
i) After stabilization, well pressure (P_{well}) was reduced to 6.0 MPa at a controlled rate of 3.0 MPa/h, maintaining constant BHP to induce MH dissociation.
j) The experiment was concluded when temperature, reactor pressure, gas storage tank pressure, and balance readings had stabilized. Data was recorded every 20 s throughout the process.

The choice of the two bottom-hole pressures (6.0 and 10.0 MPa) and the depressurization rate (3.0 MPa/h) are based on past offshore NGH production tests and the limitations of the experimental apparatus, as described in Section 2 of the Supporting Information. A piston cover was employed to compact the moist Na-MMT pack using external force (see Fig. S7 in the Supporting Information). Due to the expansive nature of Na-MMT, packing

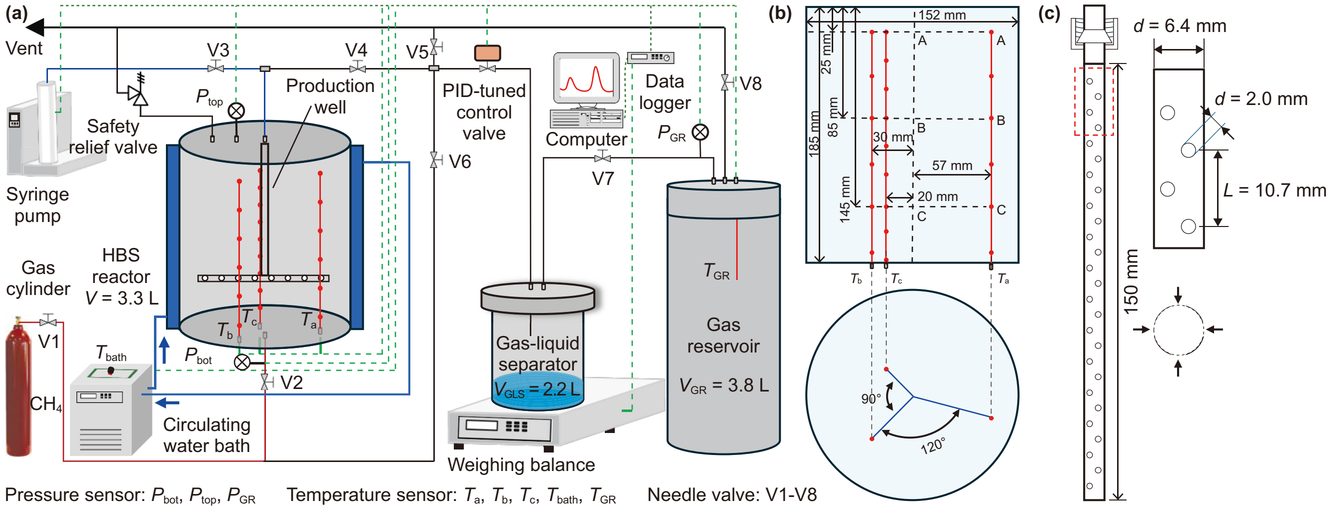

Fig. 2. **(a)** Schematic of the experimental apparatus for the synthesis and depressurization of methane hydrate-bearing sediments (MHBS) using clay layers, sand layers and clay-sand alternating layers; **(b)** cross-sectional view of the reactor showing the locations and dimensions of the temperature sensors; **(c)** design of the vertical wellbore used for depressurization.

additional clay particles into the reactor was challenging. The porosity of the Na-MMT layer after packing was ~70%, which remained representative of real clay-rich sediment conditions. According to Brown and Ransom (1996) and Tudge and Tobin (2013), the presence of abundant smectite (primarily montmorillonite) can lead to high porosity values. Indeed, the porosity of clay-rich sediments at the C0011 and C0012 sites in the Shikoku Basin (subducted in the Kumano region of the Nankai Trough) was found to reach up to ~70% (Tudge and Tobin, 2013).

The temporal evolution of phase saturations was calculated using the pore volume balance method developed in our previous work, with detailed principles and MATLAB code examples provided (Yin et al., 2020). Detailed calculation steps are provided in the Supporting Information.

3. Results and discussion

3.1. Synthesis of MHBS in clay and sand sediments

3.1.1. Evolution of P and T during MHBS synthesis

Fig. 5 illustrates the evolution of *P* and *T* during the synthesis of MHBS in Case-CS1 (clay-sand alternating layers). As shown in Fig. 5(a), after gas injection, *P* and *T* gradually stabilized at 10.3 MPa and 293.2 K, respectively. At the initial stage, the gas saturation in the reactor was approximately $S_{G0} = \sim 74\%$, and the initial water saturation was $S_{W0} = \sim 26\%$. The temperature was then lowered to 275.2 K to induce MH formation, consuming pre-mixed CBW. The S_H in the clay layer reached $S_H = \sim 13\%$, corresponding to an average reactor $S_H = \sim 9\%$ in stage A.

Once *P* and *T* stabilized, four rounds of water injection were conducted during stages B-E, with volumes of 489.09, 296.88, 132.07, and 67.11 mL, respectively. Including the pre-mixed water volume of 476.72 mL, a total of 1461.87 mL (~81.22 mol) of water was introduced during MH formation, along with an initial CH_4 amount of 6.6 mol. Therefore, the MHBS preparation followed the excess-water method. Ultimately, S_H reached ~31%, with a CH_4 conversion rate of ~60% (see Fig. 5(b)).

The evolution of phase saturations (S_i) and the distribution of three-phase saturations before MHBS depressurization were calculated using the experimental and calculation methods described in Section 2.3. The results are presented in Fig. 5(c) and summarized in Table 1. Across the experimental cases, S_H ranged from 25% to 34%. In Cases-CS2 and C2, S_H was slightly lower than in the other cases, mainly due to partial MH dissociation in the clay during the heating process, causing a small reduction in S_H (see Fig. S8 in the Supporting Information) (see Table 2).

3.1.2. MH formation characteristics from clay-bound water in clay and pore water in sand

In this study, water was pre-mixed with clay to achieve a gravimetric water content (GWC) of 40%. At this water content, all water within the clay was classified as CBW, with no free-flowing water present (see Fig. S2(b) in the Supporting Information). For comparison, a specific amount of water was added to sand samples (Case-S1) based on the gas-liquid ratio (*R*) observed in Case-C1. This approach ensured identical conditions of pressure, temperature, and liquid-gas ratio ($R = \sim 7.5$) in both Case-C1 and Case-S1, enabling a direct comparison of MH growth kinetics between CBW (Case-C1) and sand pore water (Case-S1).

As shown in Fig. 6, the *P*-*T* profiles and CH_4 uptake curves during MH formation in clay and sand with pre-mixed water were compared. The results indicate that the pressure in pure clay (Case-C1) decreased to 6.80 MPa, which was higher than the 3.40 MPa observed in pure sand (Case-S1), suggesting a lower conversion rate of CBW to MH compared to sand pore water. Furthermore, the S_H in the clay ($S_H = 14\%$) was lower than that in sand ($S_H = 29\%$).

In addition, the normalized CH_4 consumption rate during the rapid MH growth phase (denoted as t_{90}, representing the time required to complete approximately 90% of the final CH_4 conversion in this stage) was calculated. The results showed that in Case-S1 (sand layer), t_{90} was 175 min, whereas in Case-C1 (clay), t_{90} extended to 664 min, an increase of 2.8 times. The normalized CH_4 uptake rate in Case-S1 was 29.45 mmol/(mol·h), while in Case-C1, it was only 3.68 mmol/(mol·h), representing ~12.5% of the gas consumption rate in sand. These findings indicated that CBW is less conducive to MH formation compared to sand pore water (Chen et al., 2024), with both the conversion ratio and rate significantly lower.

Fig. 7 compares the spatial *T* distributions over time during MH formation in Case-C1 (clay layer) and Case-S1 (sand layer) at selected time points in formation stage A. Despite identical cooling

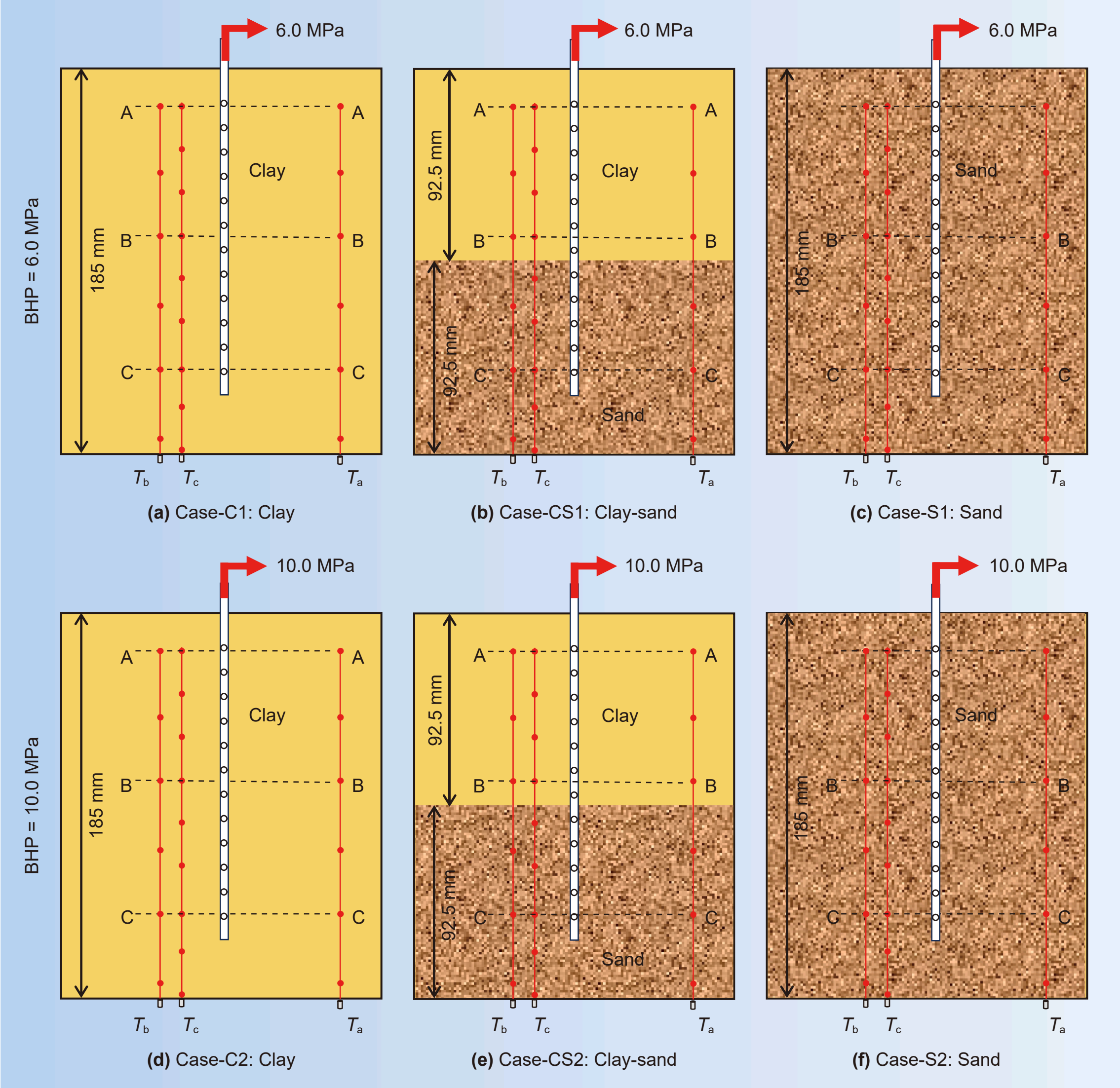

Fig. 3. Schematics of the sediment packing patterns of clay layer, clay-sand alternating layers and sand layer, and the bottom-hole pressure (BHP = 6.0 and 10.0 MPa) used in the experiment.

rates ($\Delta T/\Delta t$ = 19.7 K/h), the temperature evolution in clay and sand differed. At any given time t after cooling commenced, the average temperature (T_{avg}) in sand was consistently lower than in clay. This discrepancy is attributed to two main factors: (a) the thermal conductivity of clay (λ_{clay} = ~1.52 W/(m·K)) is lower than that of sandy sediments (λ_{sand} = ~2.75 W/(m·K)), resulting in slower heat transfer from the cooled reactor walls to the interior, and (b) the slower rate of MH formation in clay prolongs exothermic activity, maintaining a higher T_{avg} than in sand. MH formation in sand was largely completed within 300 min after cooling commenced, whereas in clay, the process extended beyond 1200 min.

3.2. Fluid production at BHP = 6.0 MPa in layered clay and sand MHBS

Fig. 8 shows the P-T trajectories and cumulative CH_4 and water production over time during depressurization in Case-CS1 (clay-sand alternating layers). As shown in Fig. 8(a), MH initially dissociated in the upper clay layer, causing a temperature drop due to the endothermic nature of MH dissociation. This effect is evidenced by a reduction in average temperatures on the A-A ($T_{A\text{-}A}$) and B-B ($T_{B\text{-}B}$) planes, manifested as an earlier inflection in the P-T trajectory compared to the sand layer (C-C plane).

The significant leftward shift of approximately 1.6 K in the P-T trajectories relative to the MH phase equilibrium curve indicates that Na-MMT thermodynamically inhibits MH formation. Consequently, under constant bottom-hole pressure (BHP) conditions, the driving force for MH dissociation represented by the pressure differential, is enhanced, consistent with previous studies (Liu et al., 2022, 2023b) and our earlier work (Ren et al., 2024). In contrast, the sand used in our experiments (particle size >100 μm) exerted minimal influence on the MH phase equilibrium (Wang et al., 2019). As a result, $T_{C\text{-}C}$ during MH dissociation remained close to the MH phase equilibrium curve, as shown in Fig. 8(a).

Due to the presence of clay, water production was limited, with R_W reaching only 6.0%, whereas R_G attained 71.8% (see Fig. 8(b)). During the early stage of MH dissociation, S_G initially decreased and then increased (see Fig. 8(c)), primarily attributed to the swelling of Na-MMT upon water absorption. Previous research indicates that during MH formation, Na-MMT shrinks as a portion

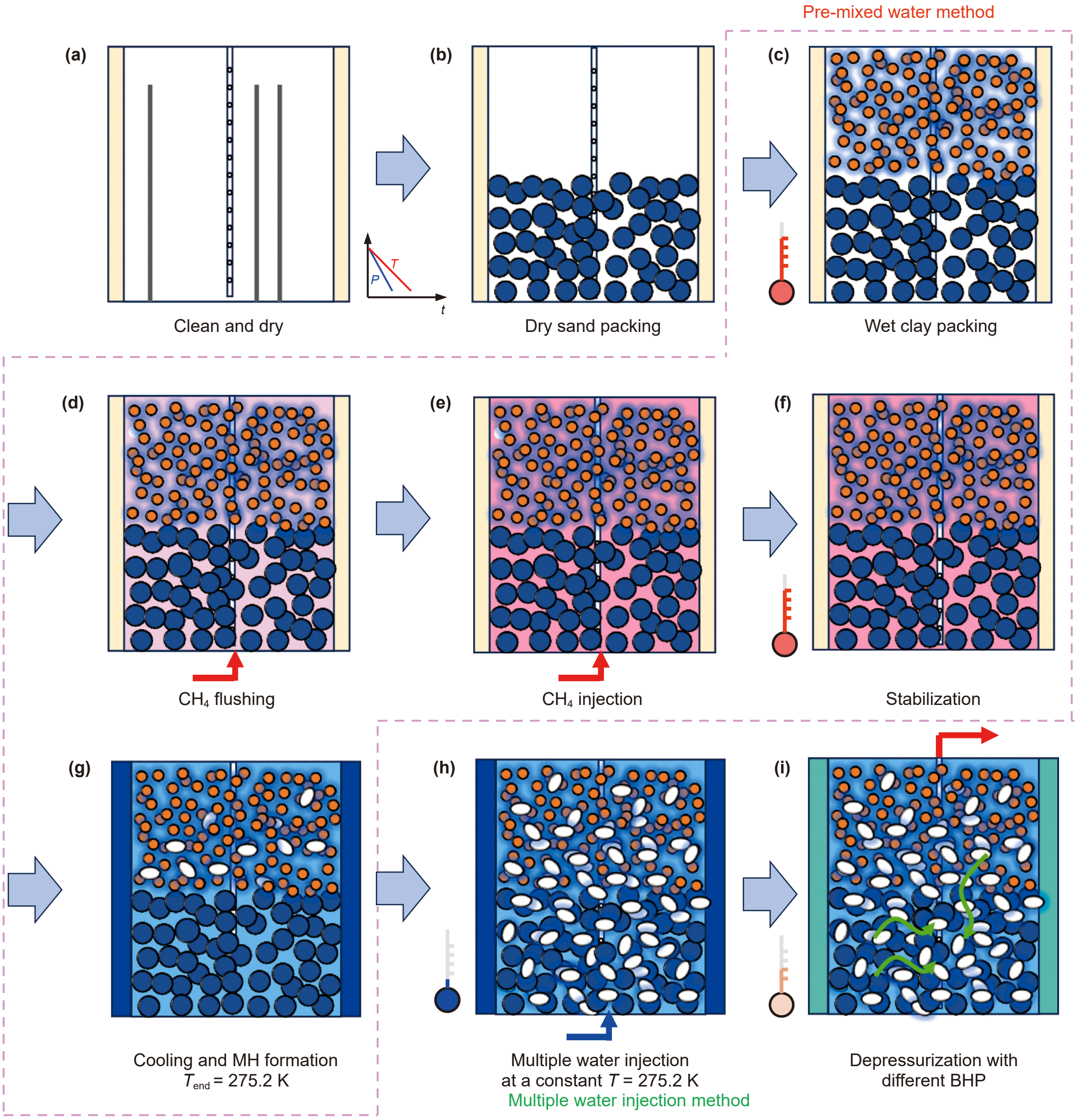

Fig. 4. Schematics showing the experimental procedure for synthesizing methane hydrate-bearing sediments in clay-sand alternating layers and the subsequent depressurization process at bottom-hole pressures of 6.0 and 10.0 MPa.

of CBW converts to MH. Ren et al. (2022a) employed low-field nuclear magnetic resonance (LF-NMR) to show that during MH dissociation, water produced was absorbed by the clay and transformed into CBW. Consequently, Na-MMT absorbs the produced water during MH dissociation, resulting in secondary swelling. This swelling trap water within the reactor, causing a rapid increase in S_W, as observed in Fig. 8(c). Simultaneously, swelling reduces pore space, expelling gas and decreasing S_G (see Fig. 8(c1)).

Fig. 8(d) presents the evolution of the water-to-gas ratio (WGR) over time. Initially, water production was relatively high, with WGR reaching approximately 1.4, resulting from the rapid expulsion of residual water during depressurization. As MH dissociation proceeded, water was absorbed by Na-MMT, leading to a gradual decrease in WGR until the end of the depressurization phase. Later, as the water absorption capacity of Na-MMT became saturated, water production gradually increased, causing WGR to rise and stabilize around 1.0 until the end of gas production.

3.3. Comparison of fluid production between sand, clay and layered clay and sand MHBS

3.3.1. Effects of BHP on gas and water recovery

The pressure variations within the reactor during depressurization are shown in Fig. 9(a) and (e). The shorter depressurization time observed in the sand layers (Cases-S1 and S2) was primarily due to the rapid initial pressure drop caused by the expulsion of water at the onset of depressurization. As shown in Fig. 9(b), when the BHP was set at 6.0 MPa, gas recovery was completed within approximately 9–10 h, with Case-S1 requiring the shortest time for MH dissociation. The time required to recover 90% of the total gas denoted as t_{D90}, was 5.3, 5.3, and 3.0 h for Case-C1, Case-CS1, and Case-S1, respectively. The differences in t_{D90} are attributed to two primary factors: (a) MH quantity in the reactor. At similar S_H levels, the clay layers and clay-sand alternating layers exhibited higher porosity (57.5%–72.8%) compared to 43.7% in the sand layer, resulting in a greater molar quantity of MH in Case-C1 and Case-

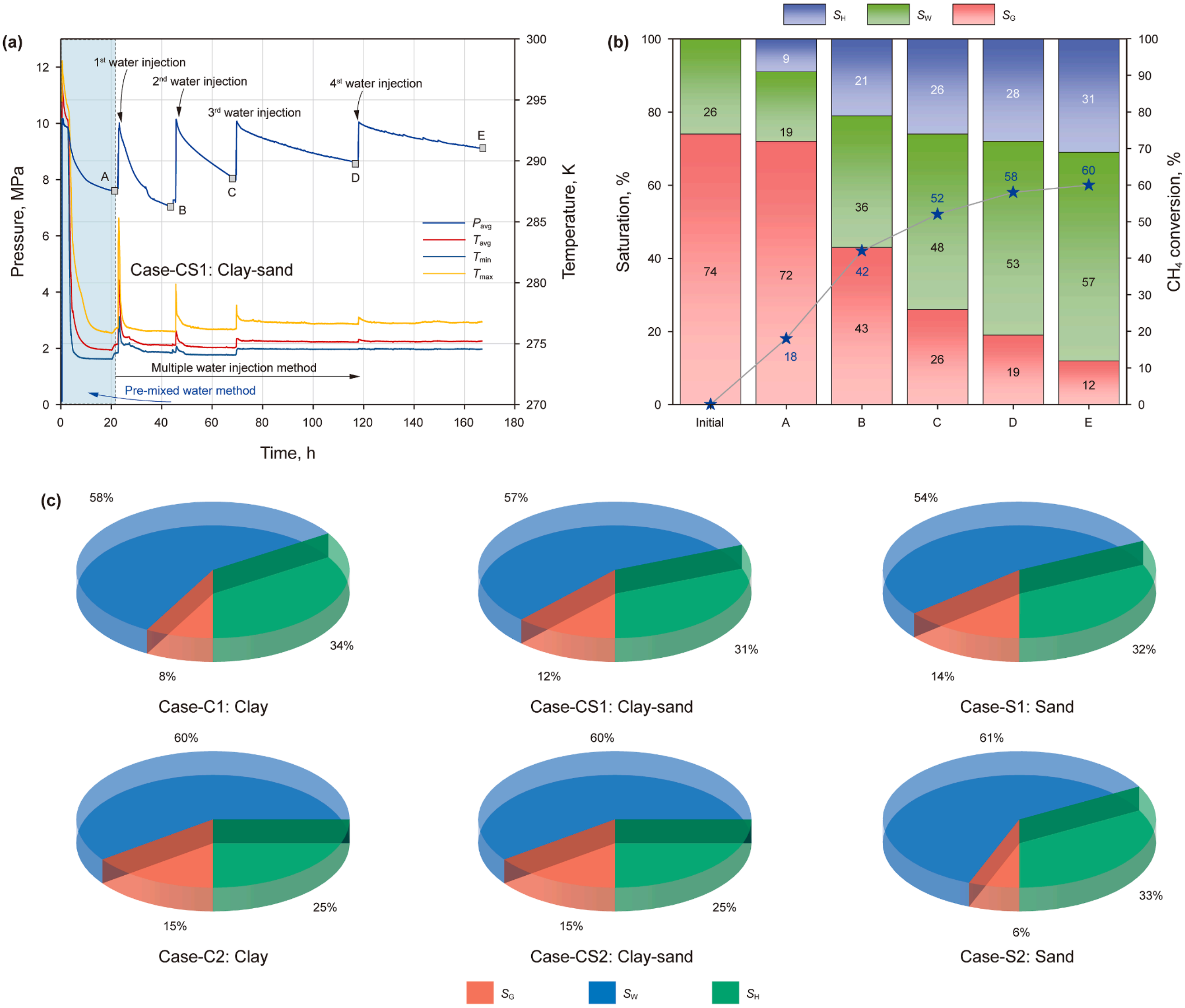

Fig. 5. **(a)** Temporal evolution of P and T over time during MHBS synthesis in Case-CS1 using pre-mixed water and multiple water injection methods; **(b)** calculated phase saturations of MH (S_H), CH_4 gas (S_G), and water (S_W), along with CH_4 conversion at the end of each MH formation stage; **(c)** summary of phase saturations in six experimental cases before depressurization.

Table 1

Summary of experimental conditions during MH formation in pack of clay layers (C1 and C2), clay-sand alternating layers (CS1 and CS2) and sand layers (S1 and S2).

Exp. No	T_0, K	P_0, MPa	m_{sand}, g	m_{clay}, g	Φ, %	$n_{G,init}$, mol	$n_{W,init}$, mol	P_{end}, MPa	T_{end}, K	S_H, %	S_W, %	S_G, %
Case-C1	293.1	10.3	0.0	2383.8	43.7	7.39	52.97	12.1	284.9	34	58	8
Case-CS1	293.4	10.0	2497.6	1191.8	57.5	6.92	26.48	11.2	284.6	31	57	12
Case-S1	293.2	10.3	4870.0	0.0	72.8	4.42	32.48	9.3	284.9	32	54	14
Case-C2	292.9	10.3	0.0	2383.8	43.7	7.38	52.97	15.2	286.4	25	60	15
Case-CS2	293.2	10.3	2497.5	1191.8	57.5	7.37	26.48	15.2	286.9	26	51	23
Case-S2	293.3	10.4	4870.0	0.0	72.8	4.43	32.59	14.2	286.8	33	61	6

CS1, which prolonged dissociation time. (b) Thermal conductivity differences between clay and sand. The thermal conductivity of water-saturated sand is higher than that of water-saturated clay. According to heat transfer principles, temperature propagation via conduction occurs faster in the sand layer, enabling more efficient utilization of the sensible heat of the reservoir. Additionally, faster water production and enhanced gas–liquid flow in sand further promote convective heat transfer, accelerating MH dissociation.

Variations in gas recovery rates were also observed. During the depressurization phase, approximately 50% of the gas was recovered in all three experiments (see Fig. 9(b)), with recovery rates of 50.2%, 53.2%, and 51.6%, respectively. The highest gas recovery rate occurred in Case-C1 (clay layer), reaching 88.4%, followed by Case-CS1 (clay-sand alternating layers) at 71.8%, while the lowest recovery rate was recorded in Case-S1 (sand layer) at only 68.3%. These differences in gas recovery were primarily attributed to the water absorption and swelling

Table 2
Summary of experimental conditions during MH dissociation at BHP = 6.0 MPa (C1, S1, and CS1) and 10.0 MPa (C2, S2, and CS2).

Exp. No	Pressure drawdown rate, MPa/h	BHP, MPa	T_D, K	T_{min}, K	P_{eq} at T_D (DIW), MPa	T_{eq} at BHP (MH), K	t_{D90}, h	R_G, %	R_W, %	WGR, mol/mol
Case-C1	3.0	6.0	284.9	279.2	8.8	281.4	5.4	88.4	4.3	0.76
Case-CS1	3.0	6.0	284.6	280.4	8.5	281.4	5.4	71.8	6.0	1.04
Case-S1	3.0	6.0	284.9	281.0	8.8	281.4	3.0	68.3	21.2	4.44
Case-C2	3.0	10.0	286.4	283.1	10.4	286.1	5.0	61.6	2.0	0.49
Case-CS2	3.0	10.0	286.9	283.6	11.1	286.1	6.5	56.9	5.4	1.04
Case-S2	3.0	10.0	286.8	285.3	10.9	286.1	8.6	43.1	23.3	8.67

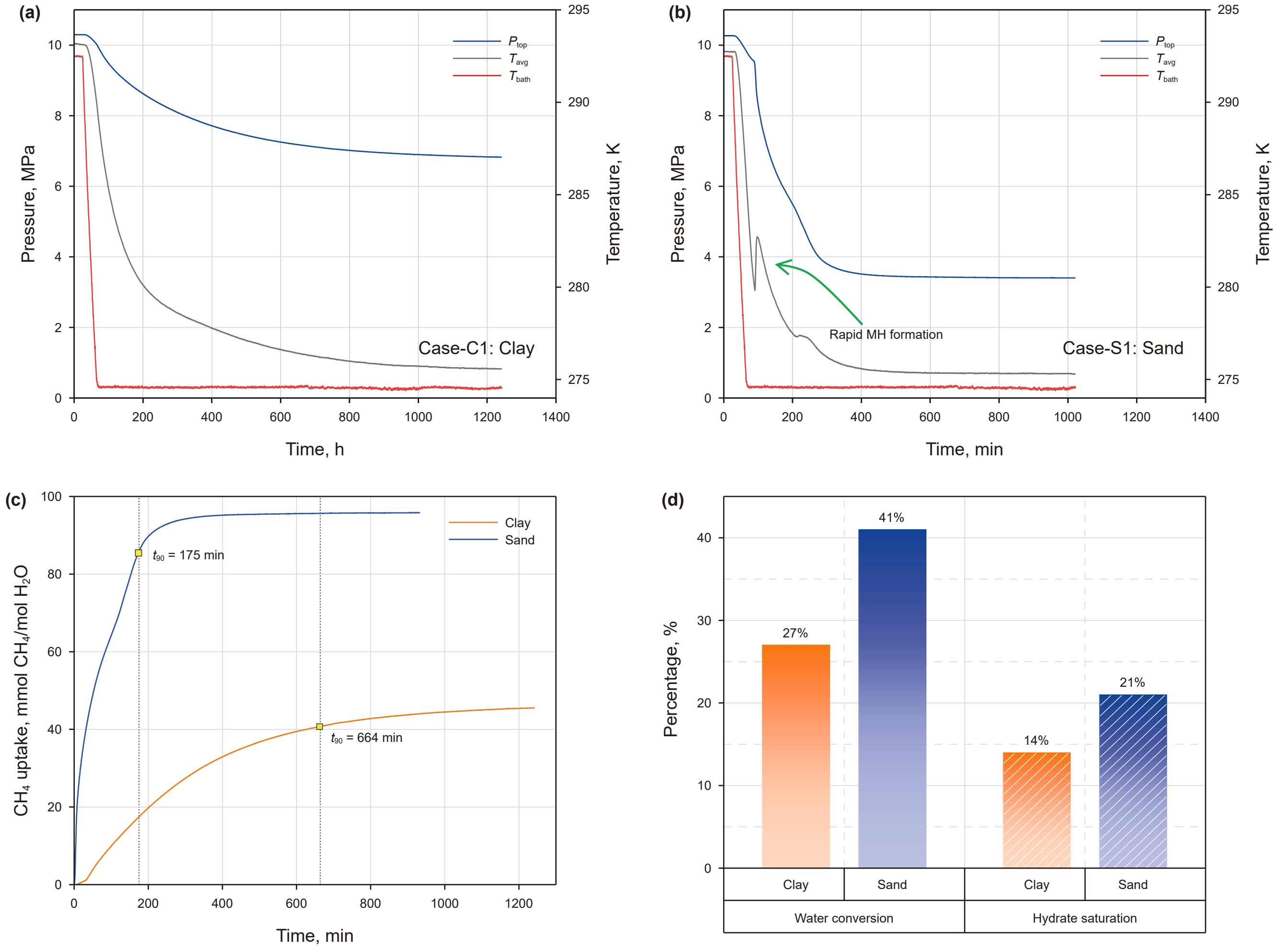

Fig. 6. Evolution of *P* and *T* over time during MH formation using the pre-mixed water method in **(a)** clay (Case-C1) and **(b)** sand (Case-S1); **(c)** comparison of CH_4 uptake between Case-C1 (clay layer) and Case-S1 (sand layer); **(d)** fraction of clay-bound water (Case-C1) and sand pore water (Case-S1) converted to MH, along with final S_H in clay and sand layers during formation stage A.

characteristics of Na-MMT. As shown in Fig. 9(c), the water recovery rate exhibited an inverse relationship with the gas recovery rate. The strong water absorption capacity of Na-MMT allowed it to retain water and occupy a larger fraction of pore space within the reactor. This absorption and the resulting swelling reduced gas saturation, thereby enhancing gas recovery. Consequently, the water recovery rate in the clay system was extremely low, with only 4.3% recovered, compared with 21.2% in the pure sand system. These differences also account for the distinct WGR trends observed in Fig. 9(d).

The gas production curves in Fig. 9(f) show that during the depressurization phase, the pure clay layer (Case-C2) achieved the highest CH_4 recovery at 61.6%, followed by the sand-clay alternating layers (Case-CS2) with a recovery of 56.9%, while the pure sand system (Case-S2) exhibited the lowest CH_4 recovery at 43.1%. Substantial differences in water production were also observed, as shown in Fig. 9(g). During depressurization, Case-S2 (pure sand) exhibited a water recovery rate of 34.4%, compared with 5.4% in Case-CS2 (sand–clay alternating layers) and only 2.0% in Case-C2 (clay layer).

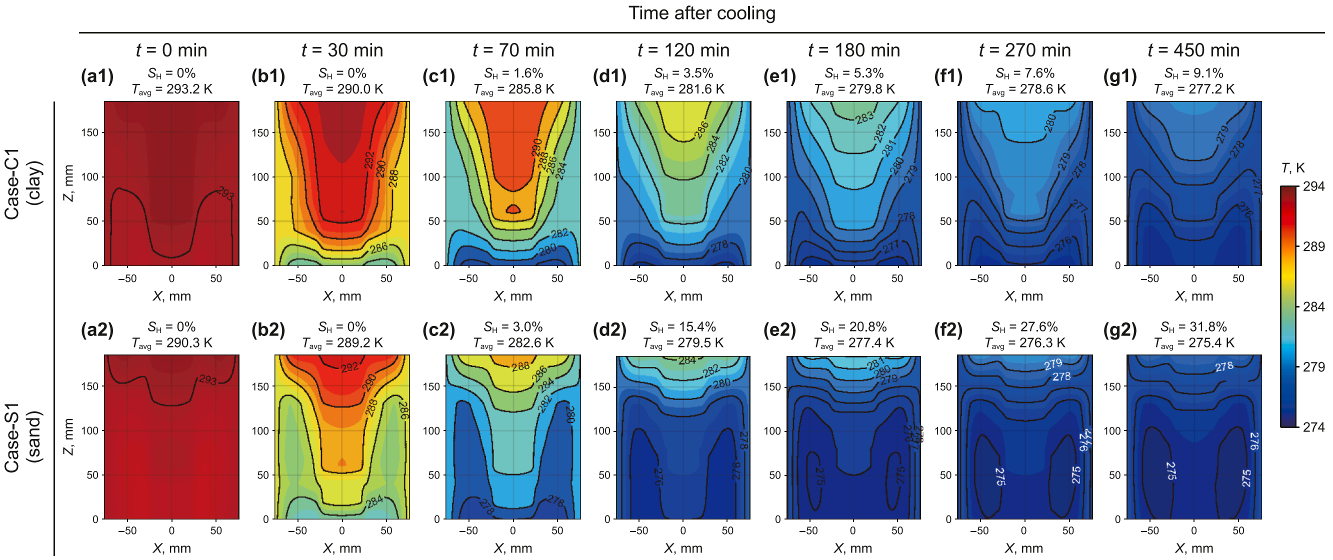

Fig. 7. Comparison of spatial T distributions over time during MH formation in the clay layer (Case-C1) and sand layer (Case-S1) at selected time points in formation stage A.

In summary, the R_G was highest in the pure clay layers (Cases-C1 and C2), and lowest in the pure sand cases (S1 and S2). However, increasing the BHP led to a reduction in R_G, decreasing from 88.4% to 61.6%. In contrast, R_W exhibited the opposite trend. Owing to the strong water absorption capacity of Na-MMT, R_W in the clay layers was only 4.3% at a BHP of 6 MPa and decreased further to 2.0% at 10.0 MPa. By comparison, water recovery in the sand systems was significantly higher, reaching 21.2% at 6.0 MPa and 23.3% at 10.0 MPa. The variation in WGR was primarily controlled by R_G and R_W (see Fig. 10). In the pure clay layers (Cases-C1 and C2), WGR was extremely low—0.76 at 6.0 MPa—and decreased further to 0.49 at 10.0 MPa, indicating that gas production far exceeded water production, with a large proportion of water absorbed and retained in the sediments by Na-MMT. When comparing R_G and R_W, the key difference under higher BHP was the reduction in R_G, whereas R_W remained nearly unchanged across the two pressures.

3.3.2. Effects of BHP on MH dissociation rate

Fig. 11(a) and (b) show that the MH dissociation rate at BHP = 6.0 MPa was higher than that at BHP = 10 MPa during both the depressurization (DP) and constant pressure (CP) stages. This difference is primarily attributed to the stronger thermodynamic driving force under the lower BHP condition. Fig. 11(b) distinguishes two stages: (a) the depressurization stage, which spans from the onset of MH dissociation until the target BHP is reached, and (b) the constant pressure stage, which begins once the target BHP is stabilized and continues until 90% of the MH has dissociated. Previous studies by Pang et al. (2009) and Zhang et al. (2024) have examined MH dissociation kinetics, identifying heat transfer and thermodynamic driving force as the dominant factors governing the dissociation process.

As shown in Fig. S9 (in the Supporting Information), the phase equilibrium curve of MH in pure clay is shifted leftward by approximately 2.0 K. This shift increases the MH dissociation driving force (represented by the temperature differential) by around 2.0 K compared with pure sand, reaching ~5.8 K—nearly twice that in sand. Consequently, a higher MH dissociation rate in clay relative to sand during both stages is expected. Interestingly, during the CP stage at BHP = 10.0 MPa, the dissociation rate in pure clay (Case-C2) was lower than that in pure sand (Case-S2), which is opposite to the trend observed at 6.0 MPa. This indicates that MH dissociation is governed not only by the dissociation driving force but also by heat transfer. Table S1 (in the Supporting Information) summarizes the dry density, thermal conductivity, and specific heat capacity of clay and sand. Calculations show that the thermal diffusivity of sand (α_{sand}) is approximately twice that of clay (α_{clay}), enabling more efficient heat transfer. As a result, sand facilitates faster temperature recovery in the reservoir, thereby accelerating MH dissociation. These observations highlight the coupled effects of dissociation driving force and heat transfer. Under a higher BHP of 10.0 MPa, the reduced driving force amplifies the influence of thermal transport properties in controlling the MH dissociation rate.

Fig. 11(c) and (d) show that a pressure differential between the reactor interior and the wellbore developed during depressurization in both Case-C1 (clay layer) and Case-CS2 (clay-sand alternating layers). This indicates that MH may partially reform around the production well, impeding pressure transmission. In Case-CS2, this pressure differential reached ~2.3 MPa and persisted throughout the depressurization process.

Additionally, we compared the real-time evolution of S_H, S_W, and S_G during MH dissociation across the different cases. Fig. 12 highlights a notable phenomenon at BHP = 6.0 MPa in the clay-containing cases (C1 and CS1). Specifically, during the initial stages of MH dissociation, S_G initially decreased and then increased. As discussed in Section 3.2, this behavior is attributed to the rapid water absorption and swelling of Na-MMT during the early dissociation phase. The swelling retains water within the reactor, leading to a rapid increase in S_W. Simultaneously, the expansion of Na-MMT occupies additional pore space, causing a sharp decline in S_G. During the CP phase, water absorption by clay (Na-MMT) stabilizes, allowing more water to be expelled from the reactor, which in turn results in a recovery of S_G.

In contrast, in Case-S1 (sand layer), water was immediately expelled at the onset of depressurization because sand lacks water absorption and swelling properties. This led to an initial rapid pressure drop (Fig. 9(a) and (e)) and a sharp decrease in S_W (Fig. 12(c) and (f)). As MH decomposed into CH_4 and water, both S_G and S_W increased, which differs from the behavior observed in the clay-containing cases. However, at BHP = 10.0 MPa, this initial decrease followed by an increase in S_G was not observed. We attribute this to the slower MH dissociation rate at 10.0 MPa,

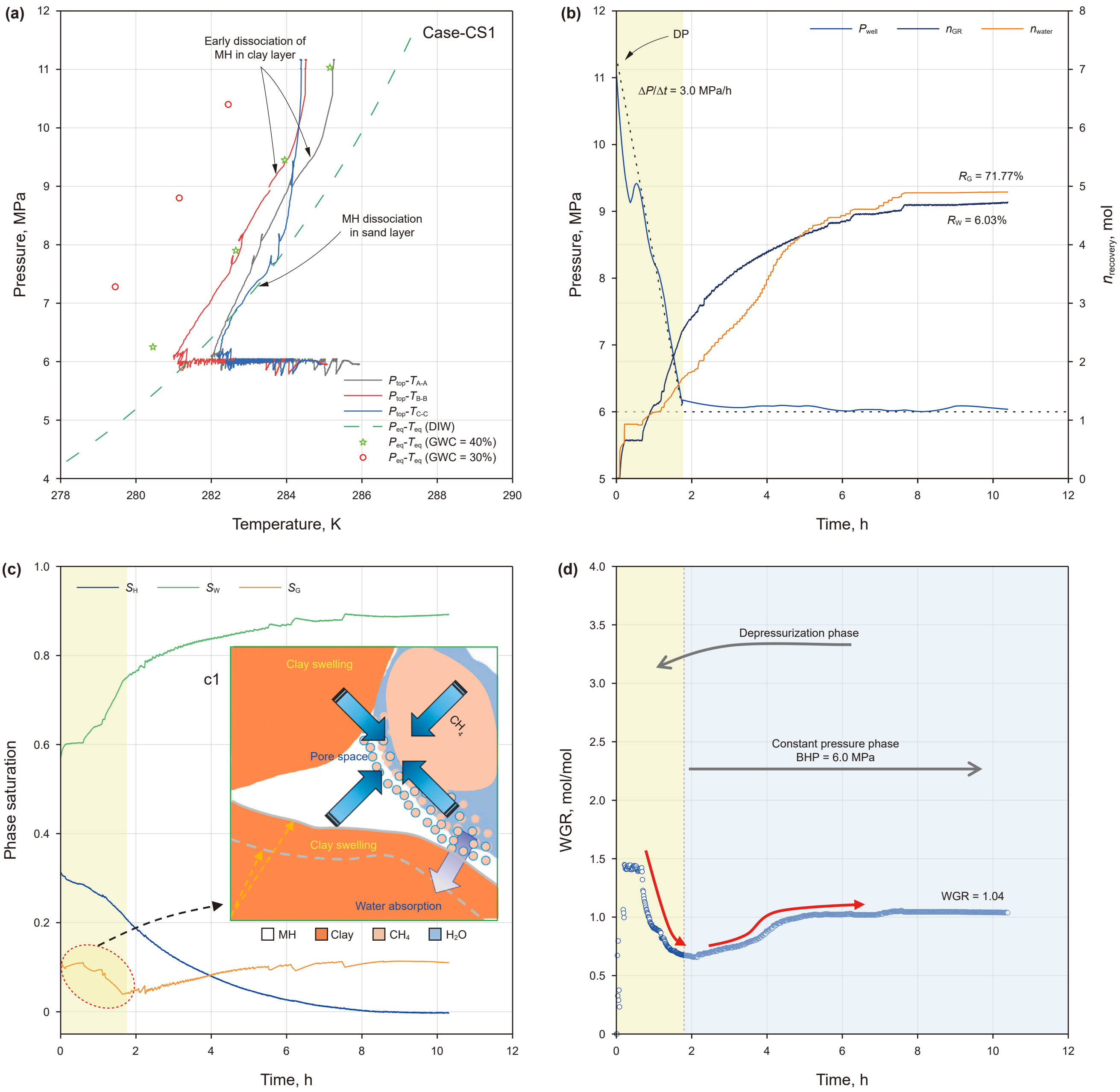

Fig. 8. **(a)** *P-T* trajectories relative to the MH phase equilibrium, with scattered points representing measured MH phase equilibria in Na-MMT with 30% (red) and 40% (green) gravimetric water content (GWC) from Ren et al. (2024); **(b)** P_{well}, cumulative production of gas (n_{GR}) and water (n_{water}); **(c)** phase saturations (S_H, S_W, and S_G) in reactor; and **(d)** water-to-gas ratio (WGR) for clay-sand alternating layers (Case-CS1) during depressurization.

which reduced the gas and water production rates. As a result, the water absorption and swelling of clay (Na-MMT) became less significant, leading to a more moderate initial increase in S_G compared with the 6.0 MPa cases (Fig. 12(d) and (e)).

3.3.3. Effects of BHP on temperature evolution

Fig. 13 presents the evolution of minimum, average, and maximum temperatures (T_{min}, T_{avg}, and T_{max}) for Cases-C1 (clay layer), CS1 (clay-sand alternating layers) and S1 (sand layer). The evolution of pressure and temperature at six specific measurement locations (T_{b1}–T_{b6}) in Case-C1 is also presented. The pressure values corresponding to the temperature spikes during depressurization phase are annotated together with the phase equilibrium temperature (T_{eq}) and the associated temperature differences (ΔT). The minimum temperatures reached in Case-C1 and Case-CS1 were 280.4 K and 279.2 K, respectively—both markedly lower than the 281.1 K observed in Case-S1. Given that the equilibrium temperature of MH at a BHP of 6.0 MPa is 281.4 K, the degree of subcooling (ΔT) was approximately 0.3 K for Case-S1, whereas ΔT ranged from 1.0 to 1.8 K in Case-CS1 and Case-C1 relative to that of pure MH. These observations are consistent with recent numerical simulations of Japan's second offshore production test at the Nankai Trough, performed using T + H v1.5 with history matching. The study identified pronounced low-temperature zones in sand-dominated layers and elevated-temperature zones in clay-dominated regions during MH dissociation. The relatively low MH concentration and low thermal diffusivity of clay-rich MHBS allow the clay-rich regions to act as a

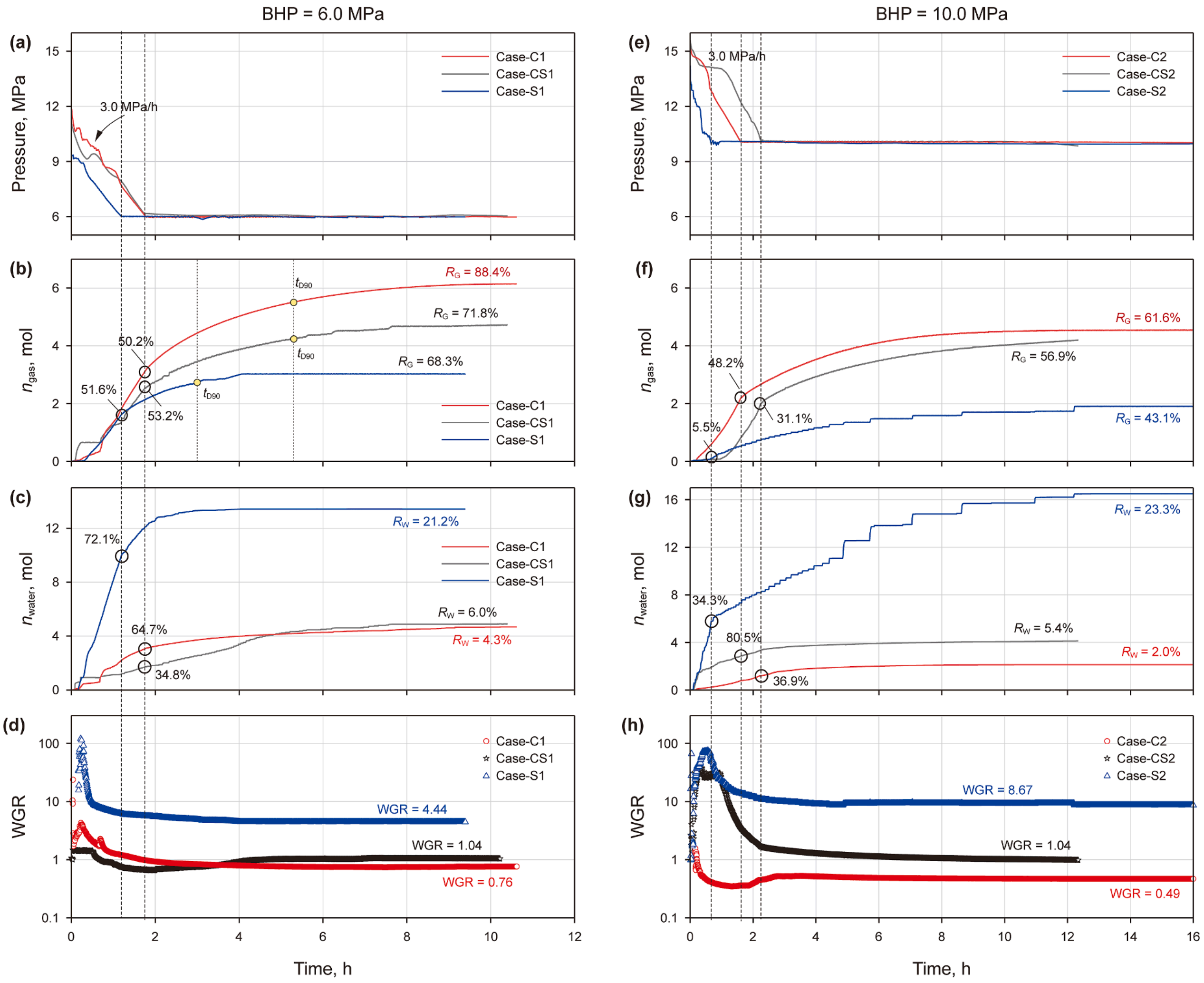

Fig. 9. Comparison of the evolution of *P*, cumulative production of gas (n_{gas}) and water (n_{water}), and water-to-gas ratio (WGR) during depressurization in clay layer (Case-C1 and C2), clay-sand alternating layers (Case-CS1 and CS2), and sand layer (Case-S1 and S2) at a BHP of 6.0 MPa (**(a)**–**(d)**) and 10.0 MPa (**(e)**–**(h)**).

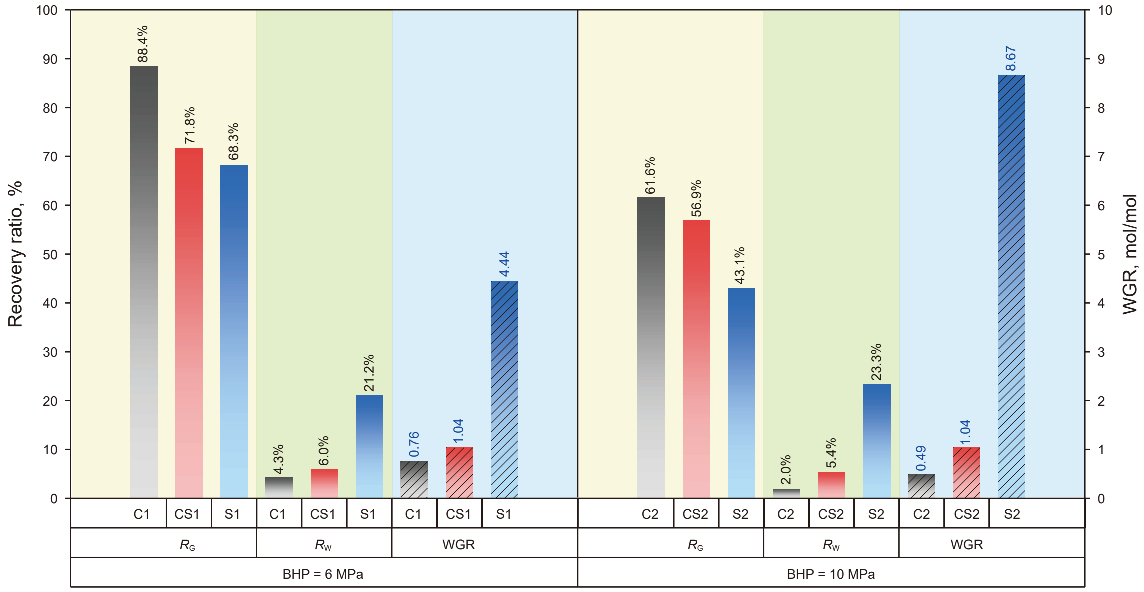

Fig. 10. Comparison of R_G, R_W, and WGR in the clay layer (Cases-C1 and C2), clay-sand alternating layers (Cases-CS1 and CS2), and sand layer (Cases-S1 and S2) at BHP = 6.0 and 10.0 MPa.

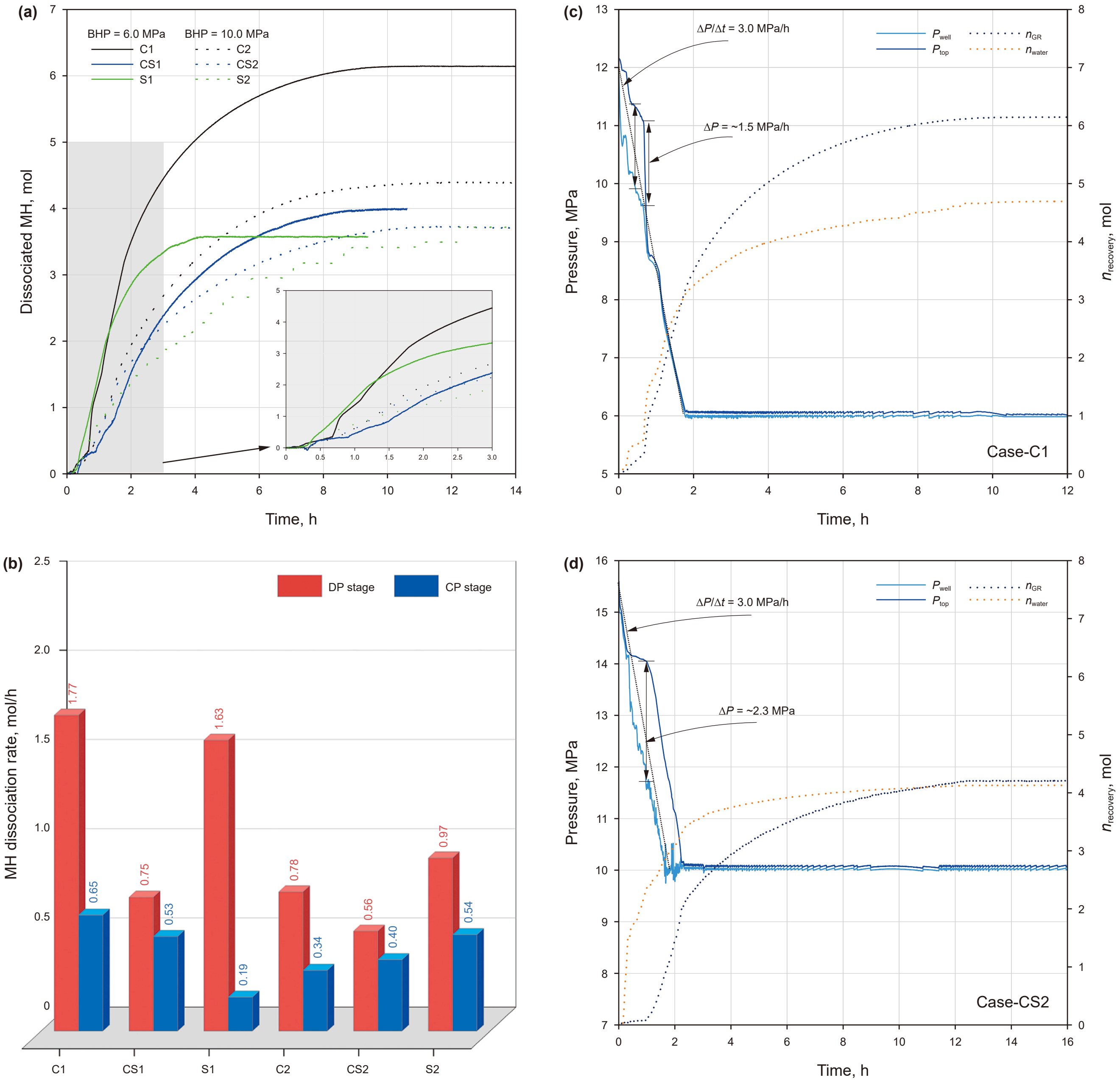

Fig. 11. (a) Dissociated MH over time across six experimental cases; **(b)** dissociation rate of MH during the depressurization and the constant pressure stage. Evolution of reactor pressure (P_{top}), well pressure (P_{well}), cumulative production of gas (n_{GR}) and water (n_{water}) in **(c)** Case-C1(clay layer) and **(d)** Case-CS2 (clay-sand alternating layers).

thermal insulation layer during CH_4 recovery at field scale, supplying sensible heat to adjacent hydrate-bearing sand layers and thereby enhancing MH dissociation (Li et al., 2025).

MH reformation was observed in clay-containing cases (Cases-C1 and CS1). Fig. 13(b) presents the evolution of P and T (measured by the T_b sensors) in Case-C1 (clay layer). At t = 0.9 h, the connection between the reactor and the production well was established, resulting in rapid pressure equalization. During this process, gas in the reactor swiftly toward the well, causing an immediate temperature drop due to the Joule-Thomson effect. This was followed by a distinct temperature spike, indicating rapid MH reformation. The spike was recorded simultaneously by all six temperature sensors (T_{b1}–T_{b6}), confirming that MH reformation occurred quickly throughout the reactor. The corresponding degree of subcooling at this moment was approximately 2.5 K (see Fig. 13(b)). Beyond thermodynamic conditions, the enhanced MH reformation observed in clay-containing systems can also be attributed to kinetic effects. Clay minerals such as montmorillonite generate strong surface electric fields that promote MH nucleation. Furthermore, the delamination of Na-MMT particles in water produces numerous nucleation sites, thereby facilitating rapid MH reformation.

The interactions between heat transfer and MH decomposition are strongly coupled (Kou et al., 2022). Fig. 14 depicts the evolution of the spatial temperature distribution at t = 0, 30, 60, 90, 120, 190, and 500 min during depressurization, along with the corresponding average temperature (T_{avg}) and MH saturation (S_H) indicated in Case-C1 (clay layer), Case-CS1 (clay-sand alternating layers) and Case-S1 (sand layer) at BHP = 6.0 MPa. A pronounced low-temperature phenomenon was observed in Case-C1, where

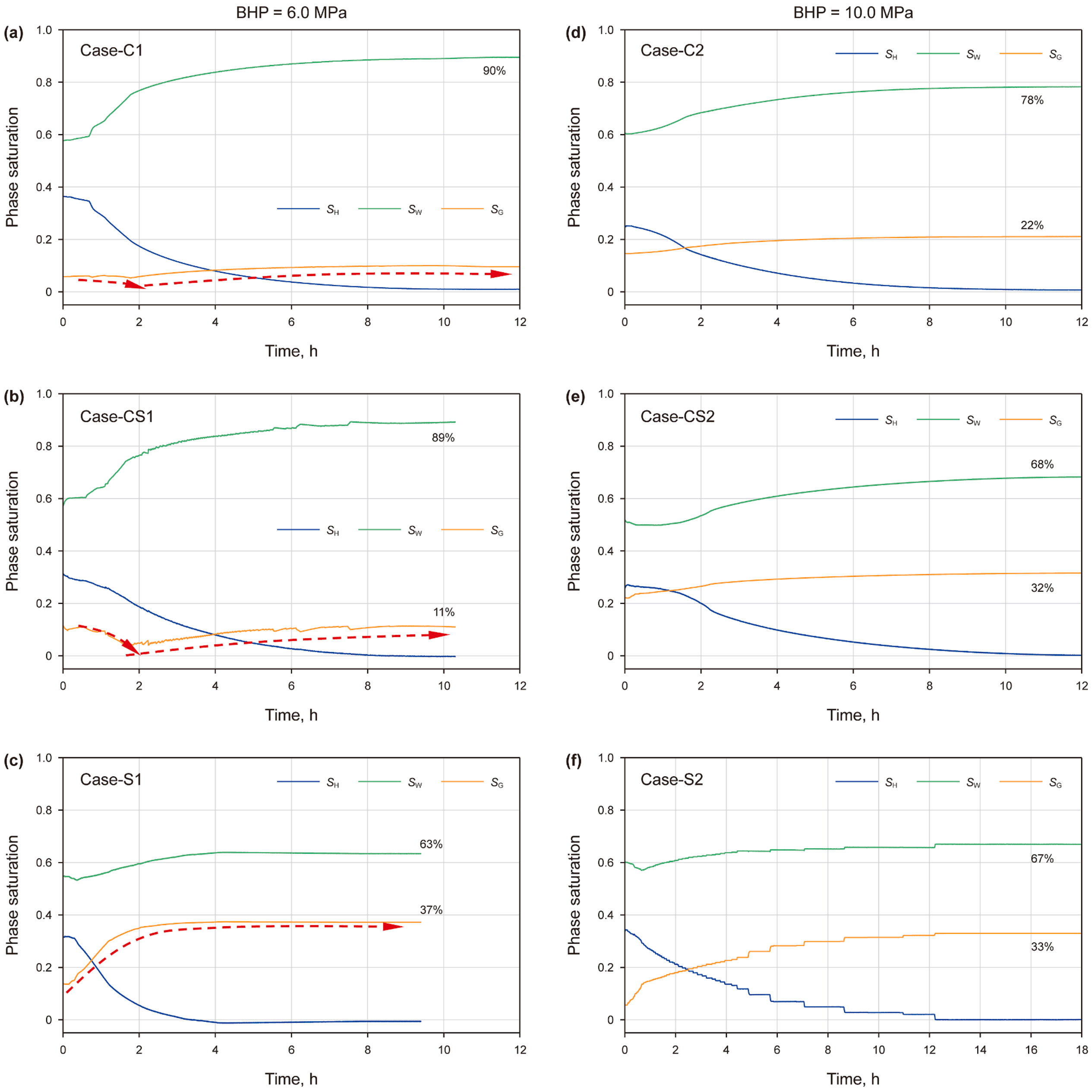

Fig. 12. Evolution of phase saturations (S_H, S_W, and S_G) in the six experimental cases: clay layers (Cases-C1 and C2), clay-sand alternating layers (Cases-CS1 and CS2), and sand layers (Cases-S1 and S2) at BHPs of 6.0 and 10.0 MPa.

T_{avg} at $t = 120$ min reached 280.2 K, approximately 1.6–2.2 K lower than in Case-CS1 and Case S1. In Case-CS1, MH dissociation within the upper Na-MMT layer was clearly evident. At $t = 60$ min, a T-drop appeared in the upper part of the reactor, and by $t = 120$ min, the temperature in the Na-MMT layer had decreased to ~281.0 K, whereas the lower sand layer exhibited temperatures between 282.0 and 283.0 K. In Case-S1 (sand layer), MH dissociation proceeded relatively rapidly, followed by prompt temperature recovery. Throughout the dissociation process, T_{avg} Case-S1 remained consistently higher than that in both Case-C1 and Case-CS1.

Significant differences in thermal physical properties between clay and sand are likely the primary factors responsible for the distinct heat-transfer behavior and the temporal evolution of temperature distributions between the clay and sand layers. Table S1 in the Supporting Information summarizes the thermal conductivity and volumetric heat capacity of water-saturated clay and sand, together with their calculated thermal diffusivity (α). Here, α denotes the thermal diffusivity (m^2/s) defined in Eq. S(10), which characterizes the rate at which heat is transferred within the clay and sand layers. Because thermal diffusivity appears as a positive coefficient in the heat Eq. S(11), it physically represents the ratio between the temporal rate of temperature change and the spatial curvature of the temperature field.

The results show that the thermal diffusivity of water-saturated clay is less than half that of water-saturated sand, indicating that the heat diffusion capacity of the clay layer is significantly lower than that of the sand layer. This difference explains the pronounced delay in temperature recovery following endothermic MH dissociation in the clay layer compared with the sand layer, as

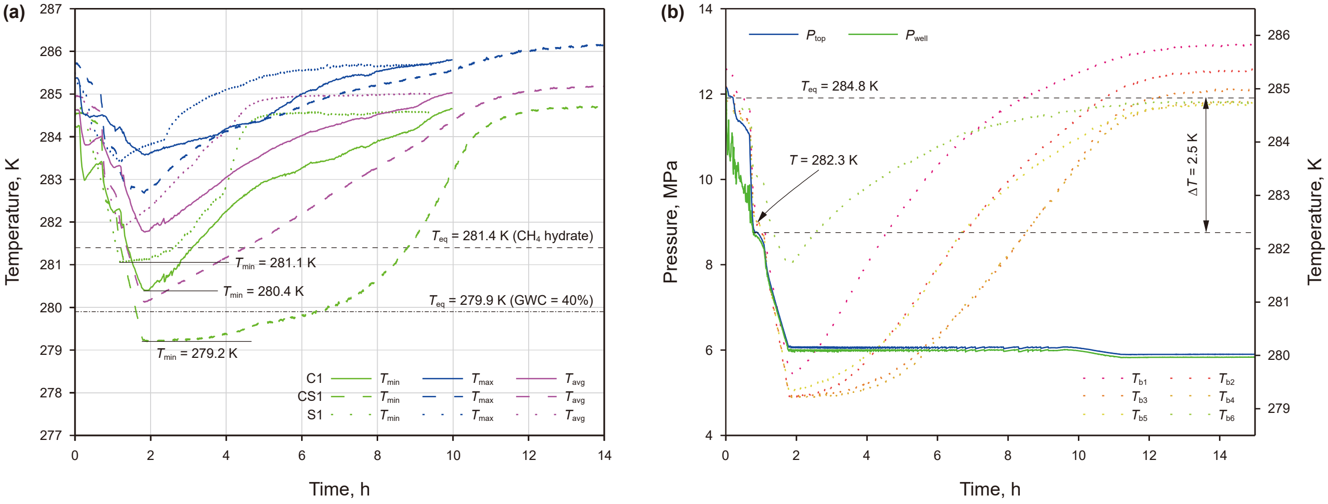

Fig. 13. **(a)** Evolution of minimum, average, and maximum temperatures (T_{min}, T_{avg}, and T_{max}) over time in Cases-C1 (clay layer), CS1 (clay-sand alternating layers) and S1 (sand layer). T_{min} values and the phase equilibrium temperature of MH (T_{eq} = 281.4 K) and of MH measured in Na-MMT (T_{eq} = 279.9 K) of GWC = 40% (Ren et al., 2024) at BHP = 6.0 MPa. **(b)** Evolution of P and T over time in Case-C1 (clay layer), with marked pressure values corresponding to temperature spikes during the depressurization phase, along with the phase equilibrium temperature (T_{eq}) and temperature differences (ΔT).

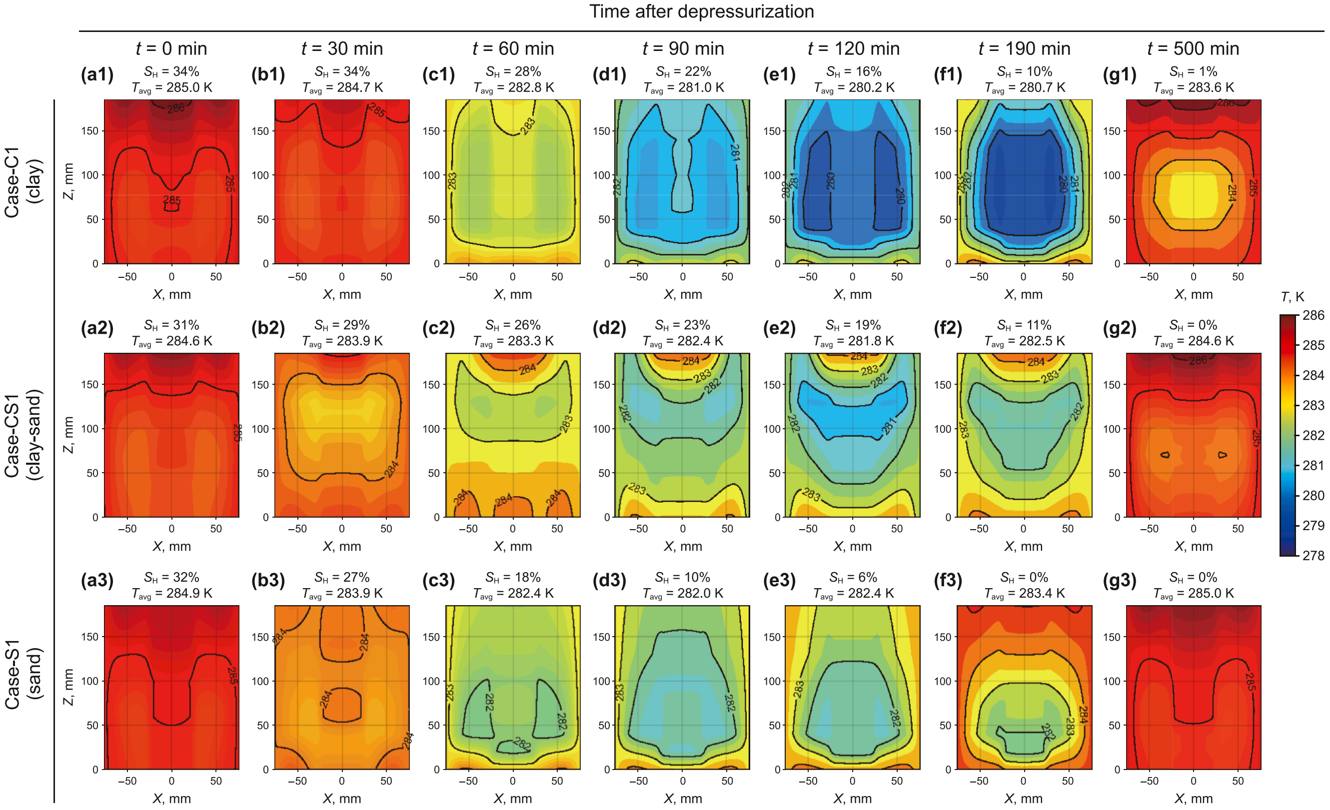

Fig. 14. Evolution of the temperature spatial distribution at t = 0, 30, 60, 90, 120, 190, and 500 min during depressurization, with the average temperature (T_{avg}) and MH saturation (S_H) indicated in Case-C1 (clay layer), Case-CS1 (clay-sand alternating layers) and Case-S1 (sand layer).

shown in Figs. 7 and 14. Fig. S11 (in the Supporting Information) the spatial temperature evolution in Case-C2 (clay layer), Case-CS2 (clay-sand alternating layers), and Case-S2 (sand layer) at a BHP of 10.0 MPa. A similar low-temperature region was observed within the clay layer (see Fig. 14(d1)–(f1) and (d2)–(f2)). Compared with BHP = 6.0 MPa, MH dissociation at 10.0 MPa proceeded more slowly, requiring a longer period for complete dissociation. The temperature in the sand layer remained relatively stable, around 286 K, further confirming that the thermal diffusivity of sand (α_{sand}) is higher than that of the clay layer (Muraoka et al., 2019; Wei et al., 2022). As a result, the sand layer maintained a more uniform temperature distribution, approximately 1–2 K lower than that of the clay layer, and no significant MH reformation was observed.

3.4. Implications

3.4.1. Implications on NGH occurrence in layered clay and sand sediments

First, the thermodynamic inhibition imposed by Na-MMT shifts the MH phase equilibrium curve toward lower temperatures. Under a typical geothermal gradient, this shift reduces the area enclosed by the seafloor, the geothermal gradient curve, and the phase equilibrium curve, thereby leading to a shallower methane hydrate stability zone (MHSZ) (see Fig. S12). Such a reduction can introduce substantial uncertainties in the estimation of NGH resources. Second, hydrate saturation in clay layers is generally lower than that in sand layers. Experimental results indicate that, under identical temperature, pressure, and gas–water ratio conditions, the conversion rate of clay-bound water (CBW) is markedly lower than that of pore water in sand. Consequently, hydrate saturation in clay is reduced because a portion of CBW is difficult to convert into MH (see Fig. 15(a)–(c)). This phenomenon is consistent with field observations from the sand–silt alternating layers during the production test in the Nankai Trough, Japan, where MH saturation in clay layers ($S_H = 0\%–10\%$) is significantly lower than in sand layers ($S_H = 50\%–70\%$) (Fujii et al., 2015).

Additionally, MH formed in Na-MMT is thermodynamically less stable and therefore prone to dissociation under minor temperature perturbations. In our experiments, MH dissociation was detected during the heating stage (see Fig. S8 in the Supporting Information). Although the heating process was completed within approximately 3 h, the system pressure continued to increase for nearly 18 h, indicating that the subsequent pressure rise resulted from MH dissociation rather than further temperature elevation. This behavior confirms that a portion of the MH formed in Na-MMT exists in a metastable state. It also explains the relatively low S_H observed in Case-CS2 and Case-C2, as part of the hydrates likely dissociated during the heating process.

3.4.2. Implications on CH_4 recovery from layered clay and sand MHBS

The phase equilibrium alteration induced by Na-MMT has direct implications for the fundamental driving force governing MH dissociation. A downward shift of 1–2 K in the phase equilibrium temperature requires corresponding adjustments to dissociation strategies. Considering a typical geothermal gradient of approximately 3.0–4.0 K per 100 m (Matsumoto et al., 2024), such a shift would translate to a reduction of tens of meters in the depth of the methane hydrate stability zone (MHSZ), which may substantially influence reservoir evaluation and production planning.

A significant presence of Na-MMT was found to enhance gas recovery while markedly suppressing water production (see Fig. 10). Our previous work demonstrated that MH formation within clay is accompanied by clay shrinkage due to the loss of clay-bound water. During subsequent MH dissociation, the released water is preferentially absorbed by Na-MMT, inducing secondary clay expansion. This expansion limits the release of free water and simultaneously displaces additional CH_4, thereby increasing gas recovery (see Fig. 15(d)–(f)). As evidenced in Figs. S10 and S11 (in the Supporting Information), Na-MMT maintains its water-absorption and expansion capacity even after MH dissociation. Upon opening the reactor following the experiments, no free water was observed, confirming that the water remained bound within Na-MMT rather than being produced as mobile liquid.

The low thermal conductivity of Na-MMT leads to the formation of low-temperature zones during MH dissociation. Coupled with the strong surface electric fields and the abundance of

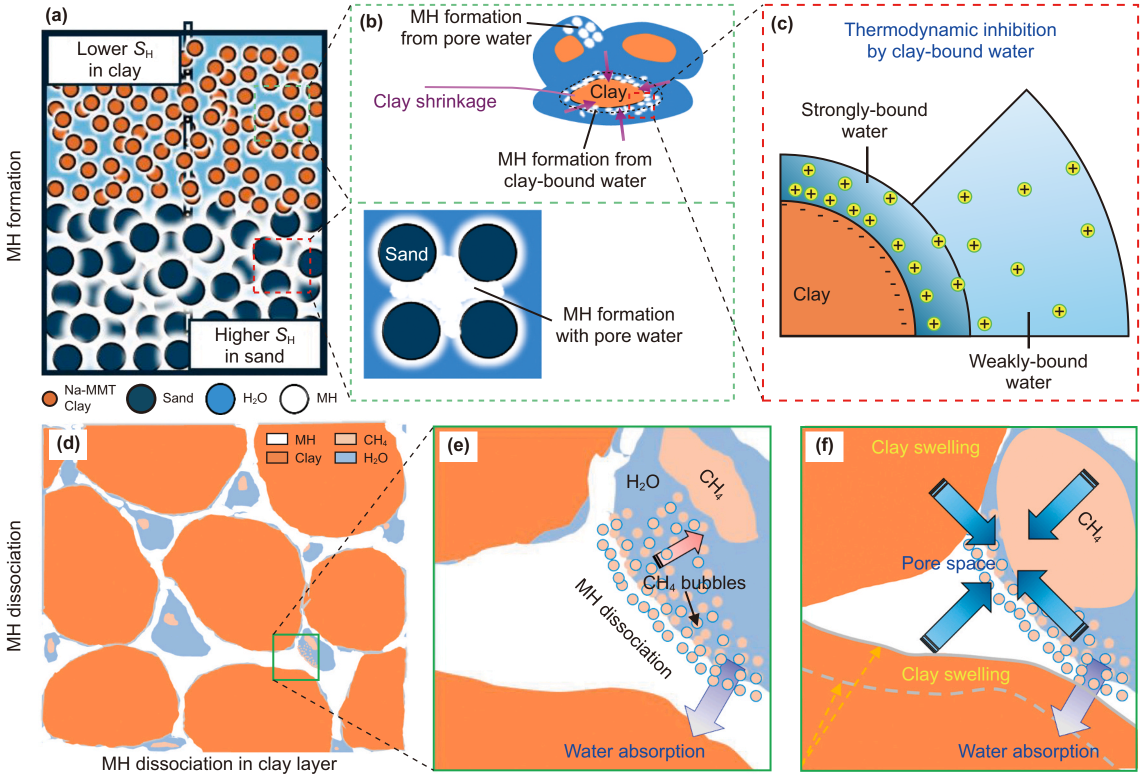

Fig. 15. A schematic showing the difference of methane hydrate formation in sand and clay layers ((**a**)–(**c**)) and how swelling of clay due to water absorption effects the distribution of CH_4 gas and water in pore space ((**d**)–(**f**)) leading to different fluid production profiles.

nucleation sites provided by Na-MMT, these conditions promote MH reformation. Such reformation not only reduces CH_4 production efficiency but also introduces potential safety hazards during reservoir exploitation.

4. Conclusions

Clay-rich host sediments are commonly present in NGH reservoirs and have been encountered in past field production tests worldwide. However, the effects of swelling clay layers on fluid production from hydrate-bearing sediments during depressurization remains poorly understood, complicating the design of optimal CH_4 recovery strategies. In this study, we developed a method to synthesize hydrate-bearing sediments in clay, sand and clay-sand alternating layers, systematically investigated the fluid production and water–gas ratio under bottom-hole pressures (BHP) of 6.0 and 10.0 MPa. Temperature evolution was analyzed in detail to assess heat-transfer characteristics. The key conclusions are summarized as follows:

1) Both the MH formation rate and hydrate saturation in swelling clay layers ($S_H = 14\%$) were significantly lower than those in sand layers ($S_H = 29\%$) under identical pre-mixed water conditions.
2) During depressurization, MH in clay layers decomposed earlier than in sand layers, due to the thermodynamic inhibitory effects of Na-montmorillonite ($\Delta T = \sim 2.0$ K).
3) Reducing BHP from 10.0 to 6.0 MPa enhanced the final CH_4 recovery for all sediment types, with clay layers reaching 88.4%, clay-sand alternating layers 71.8%, and sand layers 68.3%.
4) Swelling of clay layers through water absorption decreased water recovery to 4.3% while increasing gas recovery to 88.4%, resulting in a notably low water–gas ratio (WGR = 0.76) in clay-sand alternating layers at a BHP of 6.0 MPa.
5) Depressurization induced persistent lower-temperature zones in clay layers relative to sand layers ($\Delta T = 2.0$ °C), promoting potential MH reformation. Additionally, higher thermal conductivity in sand layers facilitated interlayer heat transfer from sand to clay, further affecting dissociation behavior.

This study provides valuable insights into fluid production from clay-rich hydrate-bearing sediments and offers guidance for the design and optimization of effective depressurization strategies in natural gas hydrate reservoirs. Future research will aim to elucidate the coupled effects of hydrate saturation, clay content, and the presence of different clay minerals on fluid production behavior under depressurization.

CRediT authorship contribution statement

Junjie Ren: Writing – original draft, Visualization, Methodology, Investigation, Formal analysis, Conceptualization. **Hongfeng Lu:** Investigation. **Chenlu Xu:** Investigation, Conceptualization. **Junjie Zheng:** Investigation. **Yue Zhang:** Investigation. **Yunting Liu:** Investigation. **Praveen Linga:** Supervision, Resources, Conceptualization. **Zhenyuan Yin:** Writing – review & editing, Supervision, Resources, Funding acquisition, Formal analysis, Conceptualization.

Declaration of competing interest

The authors declare that they have no known competing financial interests or personal relationships that could have appeared to influence the work reported in this paper.

Acknowledgements

The financial support from the National Engineering Research Center of Gas Hydrate Exploration and Development (NERCZ[202401]) is appreciated. Fundings from National Key R&D Program of China (2024YFC2814703-01) and Guangdong Basic and Applied Basic Research Foundation (2024A1515012333) are acknowledged. J. R. would like to acknowledge the support provided by China Scholarship Council (CSC) of China Ministry of Education. Z. Y. thank the support from Qingdao Institute of Marine Geology (KLGH-2023-01) and Guangdong Pearl River Talent Program (2021QN02H836). P. L. thank the support from Foreign Experts Project (H20250321).

Supplementary data

Supplementary data to this article can be found online at https://doi.org/10.1016/j.petsci.2026.03.029.

References

Brown, K., Ransom, B., 1996. Porosity corrections for smectite-rich sediments: Impact on studies of compaction, fluid generation, and tectonic history. Geology 24, 843–846. https://doi.org/10.1130/0091-7613(1996)024<0843:PCFSRS>2.3.CO.

Chen, C., Zhang, Y., Li, X., et al., 2024. Investigations into methane hydrate formation, accumulation, and distribution in sediments with different contents of illite clay. Appl. Energy 359, 122661. https://doi.org/10.1016/j.apenergy.2024.122661.

Cheng, L., He, R., Cui, J., et al., 2026. Microscopic insights into the fading mechanism of the hydrate memory effect. Fuel 404, 136212. https://doi.org/10.1016/j.fuel.2025.136212.

Fujii, T., Suzuki, K., Takayama, T., et al., 2015. Geological setting and characterization of a methane hydrate reservoir distributed at the first offshore production test site on the Daini-Atsumi Knoll in the eastern Nankai Trough, Japan. Mar. Petrol. Geol. 66, 310–322. https://doi.org/10.1016/j.marpetgeo.2015.02.037.

Gürsan, C., de Gooyert, V., 2021. The systemic impact of a transition fuel: Does natural gas help or hinder the energy transition? Renew. Sustain. Energy Rev. 138, 110552. https://doi.org/10.1016/j.rser.2020.110552.

Ito, T., Komatsu, Y., Fujii, T., et al., 2015. Lithological features of hydrate-bearing sediments and their relationship with gas hydrate saturation in the eastern Nankai Trough, Japan. Mar. Petrol. Geol. 66, 368–378. https://doi.org/10.1016/j.marpetgeo.2015.02.022.

Konno, Y., Fujii, T., et al., 2017. Key findings of the world's first offshore m ethane hydrate production test off the coast of Japan: toward future commercial production. Energy Fuels. 31, 2607–2616. https://doi.org/10.1021/acs.energyfuels.6b03143.

Kotchen, M., Mansur, E., 2016. Correspondence: reassessing the contribution of natural gas to US CO_2 emission reductions since 2007. Nat. Commun. 7, 10648. https://doi.org/10.1038/ncomms10648.

Kou, X., Feng, J., Li, X., et al., 2022. Visualization of interactions between depressurization-induced hydrate decomposition and heat/mass transfer. Energy 239, 122230. https://doi.org/10.1016/j.energy.2021.122230.

Li, J., Ye, J., Qin, X., et al., 2018. The first offshore natural gas hydrate production test in South China Sea. China Geol. 1, 5–16. https://doi.org/10.31035/cg2018003.

Li, P., Wang, Y., Liu, J., et al., 2025. Evaluation of carbon emission efficiency and analysis of influencing factors of Chinese oil and gas enterprises. Energy Sci. Eng. 13 (3), 1156–1170. https://doi.org/10.1002/ese3.2055.

Li, S., Gu, Y., Moridis, G., et al., 2025. Simulating Japan's second offshore natural gas hydrate field production test: insights on near-well permeability evolution. Energy Fuels. 39, 8011–8033. https://doi.org/10.1021/acs.energyfuels.5c00672.

Liu, Z., Wang, Z., Chen, L., et al., 2022. Experimental and modeling investigations of hydrate phase equilibria in natural clayey-silty sediments. Chem. Eng. J. 449, 137557. https://doi.org/10.1016/j.cej.2022.137557.

Liu, Z., Zheng, J., Wang, Z., et al., 2023a. Effect of clay on methane hydrate formation and dissociation in sediment: Implications for energy recovery from clayey-sandy hydrate reservoirs. Appl. Energy 341. https://doi.org/10.1016/j.apenergy.2023.121064.

Liu, Z., Chen, L., Wang, Z., et al., 2023b. Hydrate phase equilibria in natural sediments: Inhibition mechanism and NMR-based prediction method. Chem. Eng. J. 452, 139447. https://doi.org/10.1016/j.cej.2022.139447.

Matsumoto, R., Hiruta, A., Oi, T., et al., 2024. Overview: Distribution, occurrence, and origins of methane hydrates around the Japan Islands. J. Geogr.-Chigaku Zasshi 133, 63–89. https://doi.org/10.5026/jgeography.133.63.

Muraoka, M., Ohtake, M., Susuki, N., et al., 2019. Thermal properties of highly saturated methane hydrate-bearing sediments recovered from the Krishna–Godavari Basin. Mar. Petrol. Geol. 108, 321–331. https://doi.org/10.1016/j.marpetgeo.2018.10.037.

Pang, W., Xu, W., Sun, C., et al., 2009. Methane hydrate dissociation experiment in a middle-sized quiescent reactor using thermal method. Fuel 88, 497–503. https://doi.org/10.1016/j.fuel.2008.11.002.

Qin, X., Liang, Q., Ye, J., et al., 2020. The response of temperature and pressure of hydrate reservoirs in the first gas hydrate production test in South China Sea. Appl. Energy 278, 115649. https://doi.org/10.1016/j.apenergy.2020.115649.

Ren, J., Yin, Z., Li, Q., et al., 2022a. Pore-scale investigation of CH_4 hydrate kinetics in clayey-silty sediments by low-field NMR. Energy Fuels. 36, 14874–14887. https://doi.org/10.1021/acs.energyfuels.2c03255.

Ren, J., Liu, X., Niu, M., et al., 2022b. Effect of sodium montmorillonite clay on the kinetics of CH_4 hydrate-implication for energy recovery. Chem. Eng. J. 437, 135368. https://doi.org/10.1016/j.cej.2022.135368.

Ren, J., Yin, Z., et al., 2024. Effect of marine clay minerals on the thermodynamics of CH_4 hydrate: Evidence for the inhibition effect with implications. Chem. Eng. J. 488. https://doi.org/10.1016/j.cej.2024.151148.

Shiraishi, K., Yamada, Y., Nibe, T., 2019. Thermogenic petroleum potential of the Nankai subduction zone, offshore SW Japan. J. Petrol. Geol. 42, 417–434. https://doi.org/10.1111/jpg.12744.

Sun, Y., Jiang, S., Li, S., et al., 2021. Hydrate formation from clay bound water for CO_2 storage. Chem. Eng. J. 406, 126872. https://doi.org/10.1016/j.cej.2020.126872.

Tudge, J., Tobin, H., 2013. Velocity-porosity relationships in smectite-rich sediments: Shikoku Basin, Japan. G-cubed 14, 5194–5207. https://doi.org/10.1002/2013GC004974.

Wang, X., Wang, Y., Xie, Y., et al., 2019. Study on the decomposition conditions of gas hydrate in quartz sand-brine mixture systems. J. Chem. Thermodyn. 131, 247–253. https://doi.org/10.1016/j.jct.2018.11.009.

Wei, R., Xia, Y., Qu, A., et al., 2022. Dependence of thermal conductivity on the phase transition of gas hydrate in clay sediments. Fuel 317, 123565. https://doi.org/10.1016/j.fuel.2022.123565.

Yadav, U., Shukla, K., Ojha, M., et al., 2019. Assessment of gas hydrate accumulations using velocities derived from vertical seismic profiles and acoustic log data in Krishna-Godavari Basin, India. Mar. Petrol. Geol. 108, 551–561. https://doi.org/10.1016/j.marpetgeo.2019.02.001.

Yamamoto, K., Wang, X., Tamaki, M., et al., 2019. The second offshore production of methane hydrate in the Nankai Trough and gas production behavior from a heterogeneous methane hydrate reservoir. RSC Adv. 9, 25987–26013. https://doi.org/10.1039/C9RA00755E.

Yang, M., Chong, Z., Zheng, J., et al., 2017. Advances in nuclear magnetic resonance (NMR) techniques for the investigation of clathrate hydrates. Renew. Sustain. Energy Rev. 74, 1346–1360. https://doi.org/10.1016/j.rser.2016.11.161.

Ye, J., Qin, X., Xie, W., et al., 2020. The second natural gas hydrate production test in the South China Sea. China Geol. 3, 197–209. https://doi.org/10.31035/cg2020043.

Yin, Z., Wan, Q., Gao, Q., et al., 2020. Effect of pressure drawdown rate on the fluid production behaviour from methane hydrate-bearing sediments. Appl. Energy 271, 115195. https://doi.org/10.1016/j.apenergy.2020.115195.

Yoneda, J., Masui, A., Konno, Y., et al., 2015. Mechanical properties of hydrate-bearing turbidite reservoir in the first gas production test site of the Eastern Nankai Trough. Mar. Petrol. Geol. 66, 471–486. https://doi.org/10.1016/j.marpetgeo.2015.02.029.

Yu, T., Guan, G., Abudula, A., 2019. Production performance and numerical investigation of the 2017 offshore methane hydrate production test in the Nankai Trough of Japan. Appl. Energy 251, 113338. https://doi.org/10.1016/j.apenergy.2019.113338.

Zhang, J., Yin, Z., Khan, S., et al., 2024. Path-dependent morphology of CH_4 hydrates and their dissociation studied with high-pressure microfluidics. Lab. Chip 24, 1602–1615. https://doi.org/10.1039/D3LC00950E.